Morphological Expression of the Coherence and Relative Phase of Optical Inputs to the Photoelectrodeposition of Nanopatterned Se–Te Films

Azhar I. Carim,[†] Nicolas A. Batara,[‡] Anjali Premkumar,[‡] Richard May,[†] Harry A. Atwater,[‡,§] and Nathan S. Lewis*,[†,§,⊥]

[†]Division of Chemistry and Chemical Engineering, [‡]Division of Engineering and Applied Sciences, [§]Kavli Nanoscience Institute, and [⊥]Beckman Institute, California Institute of Technology, Pasadena, California 91125, United States

S Supporting Information

ABSTRACT: Highly anisotropic and ordered nanoscale lamellar morphologies can be spontaneously generated over macroscopic areas, without the use of a photomask or any templating agents, via the photoelectrodeposition of Se–Te alloy films. To form such structures, the light source can be a single, linearly polarized light source that need not necessarily be highly coherent. In this work, the variation in the morphologies produced by this deposition process was evaluated in response to differences in the coherence and relative

phase between multiple simultaneous linearly polarized illumination inputs. Specifically, the morphologies of photoelectrodeposits were evaluated when two tandem same-wavelength sources with discrete linear polarizations, both either mutually incoherent or mutually coherent (with defined phase differences), were used. Additionally, morphologies were simulated via computer modeling of the interfacial light scattering and absorption during the photoelectrochemical growth process. The morphologies that were generated using two coherent, in-phase sources were equivalent to those generated using only a single source. In contrast, the use of two coherent, out-of-phase sources produced a range of morphological patterns. For small out-of-phase addition of orthogonal polarization components, lamellar-type patterns were observed. When fully out-of-phase orthogonal sources (circular polarization) were used, an isotropic, mesh-type pattern was instead generated, similar to that observed when unpolarized illumination was utilized. In intermediate cases, anisotropic lamellar-type patterns were superimposed on the isotropic mesh-type patterns, and the relative height between the two structures scaled with the amount of out-of-phase addition of the orthogonal polarization components. Similar results were obtained when two incoherent sources were utilized. In every case, the long axis of the lamellar-type morphology component aligned parallel to the intensity-weighted average polarization orientation. The observations consistently agreed with computer simulations, indicating that the observed morphologies were fully determined by the nature of the illumination utilized during the growth process. The collective data thus indicated that the photoelectrodeposition process exhibits sensitivity toward the coherency, relative phase, and polarization orientations of all optical inputs and that this sensitivity is physically expressed in the morphology of the deposit.

KEYWORDS: Electrodeposition, photoelectrochemistry, photodeposition, template-free, maskless, chalcogenide
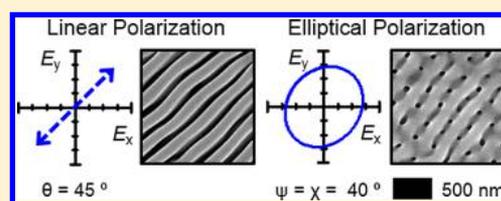
To generate a target pattern, conventional photolithography utilizes a mask to convert an isotropic light field into a structured field with a spatially varying intensity. Maskless processes, which generate structures based on anisotropic light–material interactions, provide additional routes to use illumination to effect the patterning of materials.[1] Such techniques can potentially generate unique morphologies in response to variations in properties of the optical excitation in addition to variation of the local intensity such as the wavelength, polarization, and coherence of the illumination. Such processes could provide multiple physical input parameters that may be varied simultaneously, or in combination, to direct the formation of an intended structure.[2] Exposure of metallic or semiconducting surfaces to a single highly coherent, linearly polarized laser beam can generate ordered, highly anisotropic ripple-type patterns, known as laser-induced periodic surface structures (LIPSS), wherein perio-

dicity exists in the directions perpendicular or parallel to the polarization of the incident illumination, and the characteristic period lengths are fractions of, and scale with, the excitation wavelength.[3−6] Analogous behavior has also been demonstrated for the laser-induced photodeposition of metals from organometallic precursors on metal and dielectric substrates.[7−10] Morphologies similar to LIPSS have been observed from the electrodeposition of Se–Te alloys under unstructured illumination.[11] Specifically, template-free photoelectrochemical growth of Se–Te films using linearly polarized illumination spontaneously produces deposits that display highly anisotropic, ordered morphologies. As with LIPSS, the direction of the anisotropy/periodicity is set by the polarization vector, and

the magnitude of the periodicity is a fraction of the illumination wavelength.[12,13] However, structured Se−Te deposits are produced with mW cm^{-2} intensities, whereas LIPSS formation typically requires intensities on the scale of kW cm^{-2} or MW cm^{-2}. Generation of LIPSS also requires the use of a highly coherent illumination source, whereas the formation of patterns via the photoelectrochemical process proceeds even with highly incoherent light sources. For example, equivalent photoelectrodeposit morphologies have been observed when the illumination was provided by a HeNe laser or by a highly incoherent, broadband tungsten-halogen lamp.[13] Patterning of nm scale features over cm scale areas via the photoelectrochemical process has been observed.[11] This observation, along with the observation that such patterning may be effected with a low intensity, highly uncorrelated, broadband source, suggests it may be possible to effect nanoscale patterning over much larger scale areas via this method, possibly by capitalizing on the apparent compatible nature of solar insolation.[13]

The morphologies of Se−Te photoelectrodeposits generated using two same-wavelength illumination sources have been investigated herein with a series of discrete linear polarizations in tandem, either both mutually incoherent or mutually coherent with defined phase differences. In conjunction with the experiments, the morphologies of the resulting deposits were simulated by computational modeling of the light−material interactions intrinsic to the photoelectrochemical growth process. This collective assessment examines the capacity of the deposition process to generate unique morphologies in response to discrete net polarization states and thus to display sensitivity toward the coherency, phase difference, and polarization orientations of the optical inputs. Such further elaboration of the relationship between the illumination and resultant morphology enables the use of deliberately tailored excitation to effect the programmable growth of the deposited material. Additionally, the encoding of optical input polarization and relative phase in nonvolatile physical media is immediately relevant to advanced polarization holography. In this technique, data is written by using two polarized optical beams with arbitrary phase differences in summation to generate unique morphologies that are characteristic of the polarizations and relative phases of the writing beams. Polarization holography can provide significantly higher volumetric data storage capacity than conventional holography and thus is of potential interest for application in high density optical storage of digital data.[14−16]

Se−Te photoelectrodeposits were generated using illumination from a single light-emitting diode (LED) source that had an intensity-weighted average wavelength, λ_{avg}, of 630 nm and that was linearly polarized such that the E-field component was oriented at an angle θ = 45° clockwise from the vertical as indicated in the plot presented in Figure 1, panel a. Figure 1, panel b presents a representative top down scanning electron micrograph (SEM) of the deposit morphology, which reveals a highly anisotropic lamellar-type morphology wherein the long axes of the lamellae are oriented parallel to the direction of the E-field during growth.[11−13] Quantitatively, the long axes of the lamellae were oriented at 45 ± 3° clockwise from the vertical (θ_{obs}). Figure S1, panel b presents a corresponding cross-sectional SEM and indicates an average film thickness of 450 nm. Deposits were also generated in the same manner as in Figure 1, panel b, but without the use of any polarizing optic, so that the illumination was unpolarized as indicated in the plot presented in Figure 1, panel c, and representative top down and
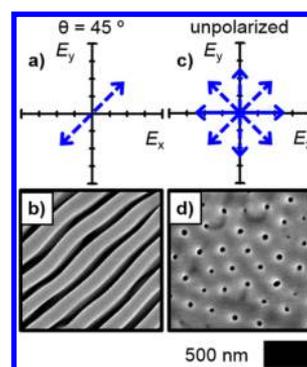

Figure 1. Effect of illumination source polarization on pattern anisotropy and orientation. (a) Plot of the E-field vector of a LED source with λ_{avg} = 630 nm linearly polarized 45° clockwise from the vertical, and (b) SEM representative of a photoelectrodeposit generated with this source. (c) Plot illustrative of the many E-field vectors characteristic of the same source as in panel a when unpolarized, and (d) SEM representative of a photoelectrodeposit generated with such source in the unpolarized state.

cross-sectional SEMs are presented in Figure 1, panel d and Figure S1, panel d, respectively. The use of unpolarized light resulted in the generation of an ordered, isotropic mesh-type morphology that consisted of an array of nanopores. Thus, both linearly polarized and unpolarized illumination effect material patterning, but the asymmetry inherent in the linearly polarized illumination creates morphological anisotropy and directs the orientation of the lamellae in the photoelectrodeposit.

Subsequent deposits were generated by simultaneously using two incoherent LED sources that had λ_{avg} = 630 nm and equal intensities, with the first source polarized vertically (θ_0 = 0°) and the second source offset clockwise from the vertical by θ_1 = 60°, 70°, 80°, or 90°. The E-field vectors of each of the two tandem sources are plotted for each condition in Figure 2, panels a−d. Top down and cross-sectional SEMs representative of the resultant deposit morphologies are presented in Figure 2, panels e−h and Figure S2, panels e−h, respectively. With θ_1 = 60°, a lamellar-type morphology, similar to that generated with a single illumination source, was observed (Figure 2e) with a value of θ_{obs} = 27 ± 4°. This value agrees with the intensity-weighted average polarization orientation, 0.5 × θ_1 for the conditions here, or specifically 30° for the case of θ_1 = 60°, and is consistent with behavior observed previously for 0° < θ_1 < 60°.[12] Such agreement suggests that essentially identical morphologies should be generated using either a single linearly polarized source with orientation θ or two linearly polarized sources having an average polarization orientation θ. However, when the difference between the polarization orientations of the sources increased past $\theta_1 \approx$ 60°, the morphologies observed for the use of two same-wavelength (630 nm) sources with equal intensities, but differing linear polarizations, were more complex than simple lamellar patterns (Figure 2f−h). Beyond this limit, oriented lamellae were still observed, and, for θ_1 = 70°, 80°, and 90°, θ_{obs} = 32 ± 6°, 38 ± 5°, and 46 ± 8°, respectively. The behavior is thus consistent with expectations based on the average polarization orientation. However, as θ_1 was increased, a mesh-type pattern at a height lower than the diagonal-running lamellae also became apparent (Figure 2f−h), and when θ_1 = 90° (Figure 2h), the height of this pattern approached the height of the lamellae. The cross-sectional micrographs (Figure S2f−h) directly depict the increase in height and definition of the mesh-type pattern relative to the
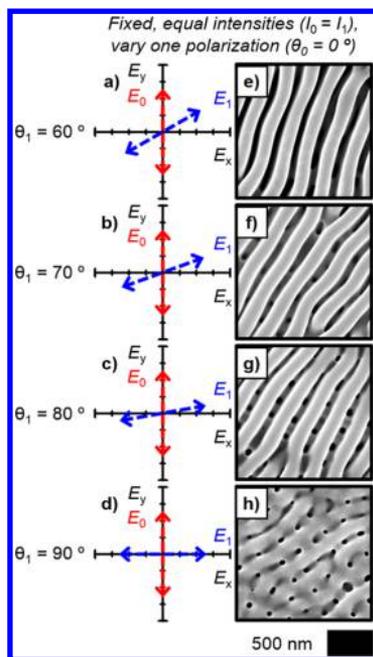
Figure 2. Two-source illumination polarization effect on photo-electrodeposit morphology for near-orthogonal and orthogonal polarizations. (a–d) Plots of the E-field vectors, E_0 and E_1, of two incoherent LED sources with $\lambda_{avg} = 630$ nm and equal intensity, the first source polarized vertically ($\theta_0 = 0°$) and the second at the indicated rotation (θ_1) clockwise from the vertical, and (e–h) SEMs representative of photoelectrodeposits generated using these sources.

lamellae with increasing values of θ_1. The morphology observed when $\theta_1 = 90°$ (Figure 2h) was not identical to that generated with a single source oriented at $\theta = 45°$ (Figure 1b), but rather it exhibited significantly less-defined anisotropy, resembling an average of the morphologies observed for the single source oriented at $\theta = 45°$ and for the unpolarized source (Figure 1d).

The appearance of the mesh-like component of the morphology, and the associated reduction of the uniaxial anisotropy, is consistent with the incoherent nature of the illumination sources utilized in these experiments. Computer modeling of the photoelectrochemical growth process was consequently performed to simulate the morphologies expected for films generated using simultaneous illumination with two coherent sources. In brief, a two-step, iterative model was utilized wherein electromagnetic simulations were first used to calculate local photocarrier-generation rates at the electrode/solution interface. In the second step, electrochemical mass addition was simulated via a Monte Carlo method that utilized the interfacial photocarrier-generation rate to thereby weight the local probabilities of mass addition. The empirical data included in the simulations were limited to literature-derived estimates of the complex index of refraction, the charge-carrier concentrations, and the excited-state lifetimes of the electro-deposited Se–Te material. Thus, the computational results were principally defined by the fundamental light–matter interactions during deposition. Simulations similar to the experiments described in Figure 2 were performed, wherein two equal-intensity sources with $\lambda_{avg} = 630$ nm were utilized, with one source polarized vertically and the polarization of the second source offset clockwise from the vertical by θ_1. However, unlike the experiment wherein incoherent sources were utilized, the simulations considered coherent sources. Simulations were performed for phase angles (ϕ) of either 0°
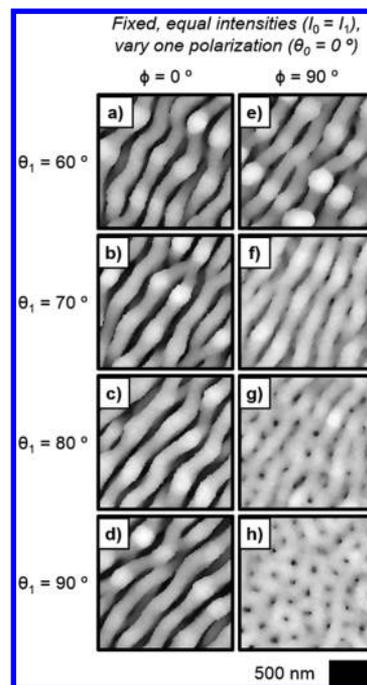

Figure 3. Three-dimensional simulations of photoelectrodeposit morphologies generated using two coherent $\lambda = 630$ nm wavelength sources with equal-intensity, the first source polarized vertically ($\theta_0 = 0°$) and the second at the indicated rotation (θ_1) clockwise from the vertical. Simulations are presented under two conditions: (a–d) one with a phase angle between the two coherent sources of $\phi = 0°$ (fully in-phase), and (e–h) with $\phi = 90°$ (fully out-of-phase). In both panels a–d and e–h, the E-field vectors of the two sources are as indicated in Figure 2, panels a–d, respectively.

or 90° between the two coherent sources. Figure 3, panels a–d present simulations for $\theta_1 = 60°$, 70°, 80°, and 90°, respectively, for $\phi = 0°$. The E-field vectors of the considered sources were identical to those plotted in Figure 2, panels a–d. In each case, a lamellar pattern was observed, and the orientation of the lamellar long axes displayed increasing rotations from the vertical with increasing values of θ_1. Specifically, values of θ_{obs} of $33 \pm 3°$, $36 \pm 2°$, $40 \pm 2°$, and $45 \pm 1°$ were measured for $\theta_1 = 60°$, 70°, 80°, and 90°, respectively. Figure 3, panels e–f present simulations analogous to those shown in Figure 3, panels a–d, but for a phase angle of $\phi = 90°$. The E-field vectors of the sources were again identical to those presented in Figure 2, panels a–d. For $\theta_1 = 60°$ (Figure 3e), the simulated morphology was lamellar and qualitatively similar to that observed with $\phi = 0°$ (Figure 3a), whereas for $\theta_1 = 70°$ (Figure 3f), the simulated morphology also displayed an oriented, lamellar-type component but appeared to be superimposed upon a mesh-type pattern. When $\theta_1 = 80°$ (Figure 3g), the lamellar pattern was less well-defined and more similar in height to the mesh-type pattern, relative to the case of $\theta_1 = 70°$. Moreover, when $\theta_1 = 90°$ (Figure 3h), the morphology lacked any apparent anisotropy and orientation and was thus similar to the morphology observed experimentally for growth stimulated by a single, unpolarized, incoherent source (Figure 1d).

The simulated morphologies displayed in Figure 3, panels a–d showed that in the case of coherent sources with a phase difference of $\phi = 0°$, only lamellar morphologies were observed. The sum of the output of two completely in-phase, coherent, linearly polarized, same-wavelength sources cannot be differentiated from the output of a single coherent, linearly polarized

source that has an equivalent net intensity and the same polarization orientation as the weighted average polarization orientation of the tandem sources. Consequently, the photo-electrodeposit morphology observed for the case of a single incoherent source polarized at θ = 45° (Figure 1b) was qualitatively matched by the simulated morphology for two equal intensity, in-phase (ϕ = 0°) coherent sources polarized at θ_0 = 0° and θ_1 = 90° (Figure 3d), with both exhibiting equivalent values of θ_{obs}. In addition, when ϕ = 0°, the measured values of θ_{obs} were equivalent to the intensity-weighted average polarization orientation, 0.5 × θ_1. In contrast, the sum of the output of two coherent, linearly polarized, same-wavelength sources that are not completely in-phase ($\phi \neq 0°$) can be differentiated from the output of a single coherent, linearly polarized source with equivalent net intensity and the same polarization orientation as the weighted average polar-ization orientation of the tandem sources. In this case, the summing of the output of the tandem sources generates elliptically rather than linearly polarized illumination. The difference in the morphologies predicted by the simulations for growths with ϕ = 0° and ϕ = 90° suggests that the photoelectrodeposition process is capable of differentiating elliptically polarized from linearly polarized illumination. Hence, the resulting photoelectrodeposit physically encodes information concerning the relative phase of the illumination inputs.

Figure 4, panels a−d present plots of the polarization ellipses that result from the out-of-phase addition (ϕ = 90°) of sources with E-field vectors the same as those plotted in Figure 2, panels a−d and thus describe the illumination utilized in the simulations presented in Figure 3, panels e−h. The orientation of the major axis of the ellipse, measured clockwise from the
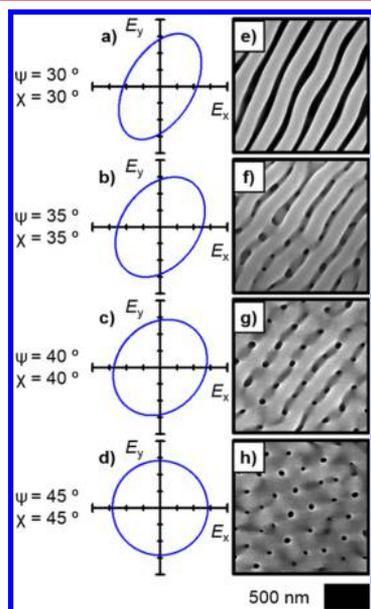
vertical, is denoted as ψ. The angle between the major axis of the ellipse and a line connecting a vertex on the major axis with one on the minor axis, denoted as χ, quantifies the asymmetry, or eccentricity, of the ellipse. For the conditions investigated in the simulations presented in Figure 3, panels e−h, $\psi = \chi$ = 0.5 × θ_1. By using these same elliptical polarizations, deposits were generated experimentally (with HeNe laser illumination with λ_{avg} = 632.8 nm) to corroborate the conclusions from the simulations that the photoelectrochemical growth process can discriminate between linearly and elliptically polarized illumi-nation and thus responds to phase data contained in the incident illumination. The growth modeling indicated that this phenomenon manifests itself in the degree of nanoscale pattern anisotropy and is potentially an effect of variable anisotropy in the illumination polarization. The addition of out-of-phase orthogonal polarization components results in the generation of an elliptical polarization state, and increasing amounts of such components decrease the asymmetry of the relevant polar-ization ellipse (quantified by χ). The simulations predict that as this asymmetry is reduced beyond a threshold ($\chi > 30°$), the observable morphological patterning begins to transition from anisotropic to isotropic, and, in the limiting case of circular polarization (χ = 45°), the patterning becomes completely isotropic.

Figure 4, panels e−h present SEMs of the deposits that were generated utilizing the elliptical polarizations corresponding to those presented in Figure 4, panels a−d. Corresponding cross-sectional SEMs are presented in Figure S3, panels e−h. Deposition with elliptical polarization with χ = 30° (Figure 4e) resulted in the generation of lamellar structures with highly uniaxial anisotropy, as in the case of linear polarization (Figure 1b; χ = 0° equivalent). For χ = 35° (Figure 4f), the overall morphological anisotropy was reduced compared to the case for χ = 30°, and an isotropic mesh-type pattern was observed underlying the anisotropic lamellar pattern. For χ = 40° (Figure 4g), this mesh-type morphology became more prominent, with a height approaching that of the anisotropic pattern. For χ = 45° (Figure 4g), no anisotropic pattern was observed; rather, the morphology was highly similar to that produced by a single unpolarized incoherent source (Figure 1d). Thus, the experimental morphologies presented in Figure 4, panels e−h matched those predicted by the growth model (Figure 3e−h). Such collective agreement demonstrates the capacity of the deposition to produce unique morphologies in response to elliptically polarized illumination and thus to store relative phase information. Specifically, superimposed isotropic mesh-type patterns and anisotropic lamellar-type patterns are generated wherein the weighting between the two types of patterns is correlated with the phase difference between the orthogonal polarization components of the optical field (and thus the resultant ellipticity of the output).

Auxiliary information regarding the polarization state of the incident illumination is also inherent in the lamellar-type pattern because the pattern anisotropy is associated with an orientation. To characterize the relation between an elliptical polarization and the encoded orientation, additional deposits were generated experimentally using polarizations having 0° ≤ ψ ≤ 25° and $\chi = \psi$. Figure 5, panel a presents values of θ_{obs} for 0° ≤ ψ ≤ 40° (wherein $\chi = \psi$) as a function of ψ. The trend is well-fit by a line of the form $\theta_{obs} = \psi - 1$. Additional growth modeling was performed to generate simulated morphologies for all of the experimentally investigated elliptical polarizations. Figure 5, panel b plots the values of θ_{obs} derived from these
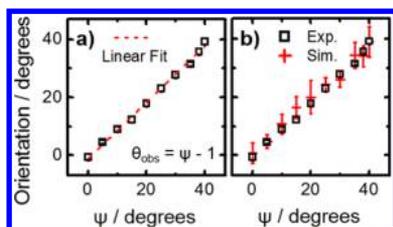

Figure 4. (a−d) Plots of the E-field vector traced over time at a fixed point for illumination provided by a HeNe laser λ_{avg} = 632.8 nm with defined elliptical polarizations. ψ indicates the orientation of the major axis of the ellipse measured clockwise from the vertical. χ represents the angle between the major axis and a line connecting a vertex on the major axis with one on the minor axis and relates the eccentricity and asymmetry of the ellipse. (e−h) SEMs representative of photo-electrodeposits generated with the elliptical illumination profiles indicated in panels a−d, respectively.

Figure 5. (a) Plot of the rotation of the orientation of the long axis of the pattern (θ_{obs}) measured clockwise from the vertical as a function of ψ for photoelectrodeposits generated with elliptically polarized illumination. Error bars generally smaller than displayed symbols. (b) Same as panel a but with addition of values derived computationally from growth modeling.

Figure 6. Flowchart detailing expected morphology of the photoelectrodeposit as a function of the polarization characteristics of the optical inputs. θ represents the angle between the polarization vectors of two linearly polarized inputs, and φ represents the phase angle between two coherent inputs. Simultaneous inputs are assumed to be of equal intensity. Anisotropic morphologies orient with long axes parallel to the average polarization vector of the input(s).

simulations as a function of ψ, along with the corresponding experimental observations. Quantitative agreement was observed between the simulation and experiment. The near equivalence between θ_{obs} and ψ indicates that the directional component of the anisotropy of an elliptical polarization state is directly recorded in the deposit morphology. Moreover, this anisotropy is discernible not only when the polarization is defined by a highly asymmetric ellipse (small values of χ, approximating linear polarization), but also when the polarization is defined by a near-circular ellipse, for example, $\chi = 40°$ (Figure 4h). This behavior indicates that when the illumination used in the deposition process is supplied by tandem sources, the lamellar component of the morphology arises from the in-phase addition of orthogonal polarization components, whereas the mesh component arises from out-of-phase addition. This behavior and rationale also are consistent with the observations of the morphologies generated using two near-orthogonal or orthogonal equal intensity incoherent sources (Figure 2). As observed for the analogous simulations (Figure 3e−h) and experiments (Figure 4e−h) with coherent sources with $\phi = 90°$, only a lamellar-type morphology was observed for $\theta_1 = 60°$ ($\theta_0 = 0°$), whereas a lamellar-type morphology superimposed on a mesh-type was observed for $\theta_1 = 70°$ and $80°$. In each case, the lamellar morphology was oriented along the intensity-weighted average polarization orientation. However, in contrast to deposits generated using coherent sources with $\phi = 90°$, the lamellar morphologies were more prominent for $\theta_1 = 70°$ and $80°$, and for $\theta_1 = 90°$, some anisotropy was still observed. This behavior results from the presence of in-phase addition in complement to the out-of-phase addition solely present in the coherent with $\phi = 90°$, as the summing of the incoherent sources involves many additions with a continuous range of phase angles ($0° \leq \phi \leq 90°$), in contrast to the coherent case for which ϕ was fixed at $90°$. Similarly, the absence of a discernible mesh-type morphological component in the incoherent case with $\theta_1 = 60°$ is consistent with an insufficient amount of out-of-phase addition of orthogonal polarization components.

Figure 6 presents a flowchart that outlines the expected morphology of the photoelectrodeposit as a function of the polarization characteristics of the optical inputs. In summary, photoelectrodeposition using a single, linearly polarized source resulted in the generation of a highly anisotropic, lamellar-type morphology, whereas the use of an unpolarized source resulted in the generation of an isotropic, mesh-type morphology. The use of tandem simultaneous same-wavelength, linearly polarized, coherent and in-phase sources also resulted in the generation of lamellar-type structures because such illumination
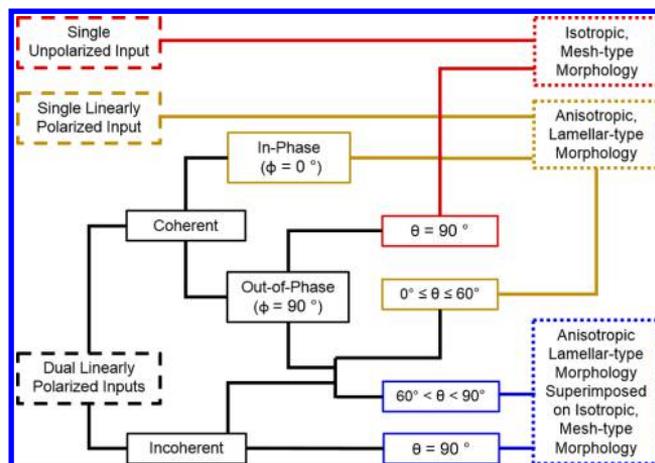
is equivalent to that produced by a single linearly polarized coherent source. Summing two linearly polarized, coherent sources that are not completely in-phase results in elliptically polarized illumination. The use of such illumination generated a spectrum of related morphologies that were dependent on the ellipticity, which correlates with the amount of out-of-phase addition between orthogonally polarized components of the optical inputs. For sufficiently low degrees of ellipticity ($\chi \leq 30°$), lamellar morphologies that appear equivalent to those generated using a single linearly polarized source were observed. For greater degrees of ellipticity, lamellar-type patterns were superimposed on a mesh-type pattern that was similar to the pattern observed when unpolarized illumination was used. Relative to the lamellar-type pattern, the mesh-type pattern increased in height and definition as the degree of the polarization ellipticity increased. Only the mesh-type pattern was observed in the limiting case of circular polarization ($\chi = 45°$). The results of deposition using two linearly polarized, incoherent sources were consistent with those observed for the use of two coherent sources that were not completely in-phase in that anisotropic, lamellar-type morphologies transitioned to isotropic, mesh-type morphologies as the amount of out-of-phase addition increased between the orthogonally polarized components of the light sources. When tandem sources were used and lamellar-type morphologies were generated, the long axis of the lamellar pattern always aligned parallel to the intensity-weighted average polarization orientation. The observed morphologies consistently matched those simulated by computational modeling, indicating that the specific morphology was fully determined by each set of defined optical inputs. Thus, the collective experimental and computational modeling data indicate that the photoelectrochemical growth process is sensitive to the coherency, relative phase, and polarization orientations of the utilized illumination inputs and that the resulting morphology expresses these inputs in a distinctive pattern in each case.

■ ASSOCIATED CONTENT

Ⓢ Supporting Information

The Supporting Information is available free of charge on the ACS Publications website at DOI: 10.1021/acs.nano-lett.5b04999.

> Additional details regarding experimental and computer modeling methods, cross-sectional micrographs, analyses of photoelectrodeposit composition and structure (PDF)

■ AUTHOR INFORMATION

Corresponding Author

*E-mail: nslewis@caltech.edu.

Notes

The authors declare no competing financial interest.

■ ACKNOWLEDGMENTS

■ REFERENCES

(1) Langille, M. R.; Personick, M. L.; Mirkin, C. A. *Angew. Chem., Int. Ed.* **2013**, *52*, 13910−13940.

(2) Destouches, N.; Crespo-Monteiro, N.; Vitrant, G.; Lefkir, Y.; Reynaud, S.; Epicier, T.; Liu, Y.; Vocanson, F.; Pigeon, F. *J. Mater. Chem. C* **2014**, *2*, 6256−6263.

(3) Birnbaum, M. *J. Appl. Phys.* **1965**, *36*, 3688−3689.

(4) Isenor, N. R. *Appl. Phys. Lett.* **1977**, *31*, 148−150.

(5) Sipe, J. E.; Young, J. F.; Preston, J. S.; van Driel, H. M. *Phys. Rev. B: Condens. Matter Mater. Phys.* **1983**, *27*, 1141−1154.

(6) Young, J. F.; Preston, J. S.; van Driel, H. M.; Sipe, J. E. *Phys. Rev. B: Condens. Matter Mater. Phys.* **1983**, *27*, 1155−1172.

(7) Brueck, S. R. J.; Ehrlich, D. J. *Phys. Rev. Lett.* **1982**, *48*, 1678−1681.

(8) Osgood, R. M.; Ehrlich, D. J. *Opt. Lett.* **1982**, *7*, 385−387.

(9) Wilson, R. J.; Houle, F. A. *Phys. Rev. Lett.* **1985**, *55*, 2184−2187.

(10) Jelski, D. A.; George, T. F. *J. Appl. Phys.* **1987**, *61*, 2353−2357.

(11) Sadtler, B.; Burgos, S. P.; Batara, N. A.; Beardslee, J. A.; Atwater, H. A.; Lewis, N. S. *Proc. Natl. Acad. Sci. U. S. A.* **2013**, *110*, 19707−19712.

(12) Carim, A. I.; Batara, N. A.; Premkumar, A.; Atwater, H. A.; Lewis, N. S. *ACS Nano* **2016**, *10*, 102−111.

(13) Carim, A. I.; Batara, N. A.; Premkumar, A.; Atwater, H. A.; Lewis, N. S. *Nano Lett.* **2015**, *15*, 7071−7076.

(14) Todorov, T.; Nikolova, L.; Stoyanova, K.; Tomova, N. *Appl. Opt.* **1985**, *24*, 785−788.

(15) Kuroda, K.; Matsuhashi, Y.; Fujimura, R.; Shimura, T. *Opt. Rev.* **2011**, *18*, 374−382.

(16) Kawatsuki, N.; Hasegawa, T.; Ono, H.; Tamoto, T. *Adv. Mater.* **2003**, *15*, 991−994.